Microstructure variation in thick AlInN films grown on *c*-plane GaN on sapphire by metalorganic chemical vapor deposition

Makoto Miyoshi[1,2]*, Mizuki Yamanaka[1], Takashi Egawa[1,2], and Tetsuya Takeuchi[3]

[1] *Research Center for Nano Devices and Advanced Materials, Nagoya Institute of Technology, Nagoya 466-8555, Japan*

[2] *Innovation Center for Multi-Business of Nitride Semiconductors, Nagoya Institute of Technology, Nagoya 466-8555, Japan*

[3] *Faculty of Science and Technology, Meijo University, Nagoya 468-8502, Japan*

*E-mail: miyoshi.makoto@nitech.ac.jp

300-nm-thick AlInN films with InN molar fractions ranging from 0.114 to 0.197 were grown by metalorganic chemical vapor deposition on *c*-plane GaN on sapphire. It was confirmed that no lattice relaxation occurred for samples with InN molar fractions from 0.144 to 0.197, and the InAlN films with low InN molar fractions showed a relative smooth surface. However, it turned into a granular surface morphology resulting from a columnar polycrystalline structure when the InN molar fraction exceeded a compositional boundary of in-plane lattice matching. As for the smooth-surface AlInN single-layers, the optical constants as well as energy bandgaps were determined.

Keywords:

B1. Nitrides, B2. Semiconducting ternary compounds, B2. Semiconducting III-V materials, A1. Crystal morphology, A3. Metalorganic vapor phase epitaxy

1. Introduction

Ternary AlInN alloys have been considered for component materials for wide variety of GaN-based electronic and optical devices [1], for examples, heterostructure field-effect transistors (HFETs) [2-5] , light-emitting diodes (LEDs) [6-8], laser diodes (LDs) [9-13], photodetectors [14,15], and waveguides [16]. In addition to their attractive bandgap nature of an extremely wide range from 0.7 eV for InN to 6.2 eV for AlN, the most distinguishing feature of AlInN is to be lattice-matched to GaN. In particular, AlInN alloys are very promising for cladding layers in visible LDs based on *c*-plane GaN, compared to conventional GaN/AlGaN superlattices or single-layer AlGaN films [17,18]. This is because cladding layers in LDs require a sufficiently-thick film with a smooth surface as well as a large index contrast to an active layer for achieving a high optical confinement factor. As for this issue, AlInN with an alloy composition lattice-matched to *c*-plane GaN, an InN molar fraction of approximately 0.17, is known to show a large index contrast in whole visible wavelength [19]. Therefore, our research group has conducted investigations on a high-quality AlInN cladding layers for achieving high-efficiency/high-power visible GaN LDs. Most recently, we grew an approximately 300-nm-thick AlInN epitaxial film with a smooth surface at a nearly lattice-matched composition to *c*-plane GaN on sapphire by metalorganic chemical vapor deposition (MOCVD) [20]. For realizing a thick and high-quality AlInN film applicable for cladding layers in LDs, further understanding of their growth mechanism is necessary. In this study, we attempted to grow and characterize thick AlInN films with different alloy compositions and then discussed the results by comparing with other researcher's results in order to understand the relationship between the growth mechanism and microstructures.

2. Experimental

AlInN films were grown on a GaN-on-sapphire template by MOCVD. Here, the GaN templates consisted of a 2-μm-thick GaN film grown on a *c*-plane sapphire substrate by MOCVD via a 30-nm-thick low-temperature GaN buffer layer. During AlInN growth, the trimethyl-aluminum, trimethyl-indium and

NH_3 gases were supplied into the reactor with a N_2 gas flow under a constant reactor pressure of 13.3kPa. To achieve different-alloy-composition AlInN films, the growth temperature was varied from 800°C to 860°C. Here, the growth time was maintained at 30 min to achieve a film thickness of 300 nm at a growth rate of approximately 0.6 μm/h. Alloy compositions of AlInN films were derived by applying lattice constants obtained from X-ray diffraction (XRD) measurements to an equation $(c - c_0) / c_0 = -2 (C_{13} / C_{33}) (a - a_0) / a_0$ [21], where, a_0 and c_0 are the room-temperature lattice constants of free-standing crystals, a and c are the measured lattice constants, and C_{13} and C_{33} are the elastic stiffness constants. Here, a_0 and c_0 of AlInN are determined according to Vegard's law [22,23] using the reported lattice constants [24], a and c were estimated using main peaks in XRD ω-2θ scans taken for symmetric (0002) and asymmetric $(10\bar{1}2)$ planes, and the elastic constants, C_{13} and C_{33}, were obtained by assuming a linear interpolation between the reported values for AlN and InN [25]. Further, X-ray rocking curve (XRC) measurement, atomic-force microscopy (AFM) and cross-sectional transmission electron microscopy (TEM) were used for evaluating the film qualities. The film thicknesses, optical constants and energy bandgaps for AlInN films were estimated using spectroscopic ellipsometry (SE) measurement.

3. Results and discussion

3.1. Relationship between the surface morphology and lattice-strain of AlInN films

Fig. 1 shows the relationship between root-mean-square (RMS) roughness and alloy compositions for 300-nm-thick AlInN films, in which typical surface AFM images are also shown. This figure obviously indicates that their surface roughness and morphology drastically varied at a specific compositional boundary. That is, samples with low InN molar fractions showed relatively smooth surface morphologies even at such a large film thickness. The surface cracks observed for a sample with the lowest InN molar fraction is probably owing to a large in-plane tensile strain. On the other hand, once the InN molar fraction exceeded approximately 0.17, however, their surfaces turned into a granular morphology and the RMS roughness

abruptly increased. The following analyses were conducted to understand this phenomenon in more depth. Figs. 2(a) and 2(b) show the lattice constants and in-plane lattice strains, respectively, obtained for different-alloy-composition 300-nm-thick AlInN films. In Fig. 2(a), *a*-axis lengths for perfectly-relaxed AlInN crystals are also drawn as a blue solid line. As obvious in the figure, *a*-axis lengths of AlInN films showed an almost constant value of approximately 3.183 Å regardless of their alloy compositions, except for the sample with cracks on the surfaces. This value is consistent with that for GaN grown on *c*-plane sapphire rather than 3.189 Å, an intrinsic value for free-standing GaN. Correspondingly, as seen in Fig. 2(b), the in-plane lattice strain linearly changed with the change in the alloy composition, except for the sample with clacks on the surface, and the in-plane lattice strain reversed its direction at a specific alloy composition. It was thus confirmed that no lattice relaxation occurred for AlInN films with InN molar fractions ranging from 0.144 to 0.197 even at a large film thickness of approximately 300 nm. Here, there is a little difference compared to results reported by Darakchieva *et al* [26]. They reported that AlInN films with InN molar fractions ranging from 0.13 to 0.18 were partially relaxed even at a film thickness of 100 nm. In this study, the partial relaxation was observed only for a sample with cracks on the surface, InN molar fraction of 0.114. As for this difference, we may have to consider the influence of growth conditions. Figs. 2(a) and 2(b) also confirm that strain-free AlInN films can be grown lattice-matched to GaN on *c*-plane sapphire when the InN molar fraction is 0.166. Further, the comparison of Figs. 1 and 2 allows to consider that the surface morphology of thick AlInN films strongly depends on their lattice strains changing along with alloy compositions. The present result indicates that an InN molar fraction lower than the lattice matching composition is appropriate to achieve thick and smooth-surface AlInN epitaxial films, as long as the crack generation does not occur. Fig. 2(b) implies that the critical in-plane tensile strain for the crack generation in 300-nm-thick AlInN films is roughly 0.3%.

3. 2. Microstructural characterization for flat- and rough-surface AlInN films

Figs..3(a) and 3(b) show sets of cross-sectional TEM bright-field images and XRD ω-2θ scanning profiles for samples with InN molar fractions of 0.164 and 0.197, respectively. For the sample with the InN molar fraction of 0.164, which is the same sample as that reported in our previous article [20] and almost perfectly lattice-matched to GaN on *c*-plane sapphire, it was confirmed to be epitaxially grown throughout whole of the thickness. In the past researches, Miao *et al* reported that 200-nm-thick AlInN films with smooth surfaces were realized within InN molar fractions ranging from 0.153 to 0.173 [27,28]. Therefore, we claim that epitaxial AlInN films with a smooth surface were achieved at a thickness greater than ever reported. In contrast to this, the other sample with the high InN molar fraction showed an obvious change in its microstructure with the increase in the film thickness. That is, it drastically turned into a columnar polycrystalline structure from an epitaxial growth mode at a film thickness boundary of roughly 100 nm or less. Thus, it was recognized that the granular morphology observed in AFM images was attributed to this columnar structure. Further, the XRD ω-2θ scanning profile obtained for the sample with the high InN molar fraction showed a distinctive sub-peak at a shoulder part of the main peak from the AlInN film, unlike that for the nearly lattice-matching sample. This implies that a phase separation occurred in the AlInN layer. To confirm the composition distribution in the AlInN layer, the energy-dispersive spectroscopy (EDS) analysis was carried out for the cross section of the film, as seen in Fig. 4. According to this analysis, indium content in an upper region of the columnar layer was observed to be a few percent less than that in the epitaxially-grown under layer.

The similar microstructures to that seen in Fig. 3(b) have been reported by previous researchers [28-31]. Some researchers also pointed out that a spontaneous phase separation occurs in AlInN films when they exceed a specific thickness boundary [26,32,33]. Although most of them discussed based on AlInN films nearly lattice-matched to GaN, we can here reconsider those reports carefully by associating them to the alloy compositions and lattice conditions. The mechanism of the microstructure transition during the growth

have been reported as follows [28,31]. That is, V-defects are first formed during the growth [34] and followed by the coalescence of those V-defects. Then, growth occurs on the inclined facets of the V-defects, which leads to the formation of a rough upper layer with a less InN molar fraction. On the other hand, Miao et al have showed an idea that the V-defects formed during the growth is related to the in-plane compressive strain, similarly to the case of GaInN [27]. Accordingly, we can consider that the results obtained this study experimentally proved the validity of their speculation. As for the growth of AlInN films with high InN molar fractions, it was concluded that there are critical thicknesses related to the in-plane compressive strain and the microstructure and composition transition occur at the thicknesses.

In order to confirm the influence of the lattice strain or polycrystallization on the crystal mosaicity, XRC measurements were carried out. Fig. 5 show full widths at half maximum (FWHMs) in XRCs for different-alloy-composition 300-nm-thick AlInN films, in which typical XRC profiles are also shown. As seen in this figure, XRC-FWHMs were found to show similar values for almost all AlInN films, such as approximately 200 s for symmetric (0002) reflections and approximately 300 s for asymmetric $(10\bar{1}2)$ reflections, respectively. These values are probably dependent on crystal quality of the underlying GaN films, in the same way as in our previous report [20]. Thus, contrary to our expectations, the XRC measurements showed no influence of the polycrystalline phases. This is probably because diffraction peaks from the polycrystalline phase were hard to detect due to their weak reflection or overlapping with strong reflections from the epitaxial phase. On the other hand, only one sample with the lowest InN molar fraction of 0.114, the partially relaxed and surface-cracked one, showed a large FWHM value for the asymmetric $(10\bar{1}2)$ reflection. This probably indicates that the partial relaxation was caused along with the generation of misfit "edge" dislocations.

For overviewing the present experimental results, critical thickness calculation was conducted according to People-Bean's (P-B's) and Matthews-Blakeslee's (M-B's) expressions. [35,36]. Fig. 6 shows calculation results for AlInN films grown on GaN on sapphire, in which the experimental data were also

plotted with brief comments. The calculation was conducted by considering only edge dislocations as misfit dislocations. As is shown in the previous sections, an alloy composition range for 300-nm-thick epitaxial growth is relatively wide for samples with in-plane tensile strain but very narrow for samples with in-plane compressive strain. In addition, the case with in-plane tensile strain seemed to be explicable with the P-B's theory, the other case with in-plane compressive strain seemed to be closer to the M-B's theoretical curves rather than P-B's. Here, both two theories consider the generation of misfit dislocations but there is a clear difference between their concepts. That is, whereas the P-B's theory focuses on the energy equilibrium, the M-B's explains by balancing the force from lattice strain and the force due to a line tension of dislocations. Further, in the P-B's expression, misfit dislocations do not appear en masse catastrophically at critical thicknesses. Generally, M-B's critical thicknesses are considered to be too thin to explain experimental results. However, in the case of AlInN films with in-plane compressive strain, it may be suitable to consider that the V-defects concurrently generate to compensate the force due to the lattice strain. Further research is needed to acquire in-depth understanding for limit of epitaxial growth.

3.3. Determination of optical constants and energy bandgaps for epitaxially-grown AlInN films

Finally, the optical constants and energy bandgaps for AlInN epitaxial films were estimated by SE analysis, in the same way as our previous work [20]. Here, the SE analyses were conducted for AlInN films with relative smooth surfaces, InN molar fractions ranging from 0.114 to 0.173. Figs. 6(a) and 6(b) show the derived refractive index n and extinction coefficient k, respectively, as a function of the incidence wavelength. The bandgap energy E_g can be estimated from the extended Tauc formula $(\alpha E)^2 \cong (E - E_g)$ [19,20,37] for photon energy E, where the light absorption coefficient α is represented by $\alpha = 4\pi k/\lambda$ using the derived k and the incidence wavelength λ. Fig. 7(a) plots the relationship between $(\alpha E)^2$ and E. Using this, the E_g is determined from the intersection of the tangent of the drawn curves with the energy axis. Fig. 7(b) summarizes the E_g values as a function of InN molar fraction in AlInN alloys together

with various researchers' results [38-44]. This figure is by updating a figure organized by Aschenbrenner *et al* [19].

4. Conclusion

In conclusion, different-alloy-composition AlInN films with a film thickness of 300 nm were grown by MOCVD on a *c*-plane GaN on sapphire template. It was confirmed that no lattice relaxation occurred for AlInN films with InN molar fraction ranging from 0.144 to 0.197. In addition, AlInN films with InN molar fractions less than 0.164 showed a relative smooth surface of less than 2 nm in RMS roughness even at such thick films. It was found that their surface turned into a granular morphology when the InN molar fraction exceeded the lattice matching composition. Cross-sectional TEM analyses confirmed that the granular surface morphology was attributed to the columnar polycrystalline structure, which was formed with a less InN molar fraction on an epitaxially-grown AlInN layer. This structural and compositional transition is probably related to the in-plane compressive lattice strain. Finally, as for the smooth-surface AlInN single-layers, the optical constants as well as energy bandgaps were derived via SE analyses.

Acknowledgement

This work was partially supported by the MEXT "Program for research and development of next-generation semiconductor to realize energy-saving society".

References

[1] R. Butté, G. Cosendey, L. Lugani, M. Glauser, A. Castiglia, G. Perillat-Merceroz, J.-F. Carlin, and N. Grandjean, in *III-Nitride Semiconductors and their Modern Devices,* ed. B. Gil (Oxford Science Publications, 2013), Series on Semiconductor Science and Technology Vol. 18, p.177.

[2] J. Kuzmik, A. Kostopoulos, G. Konstantinidis, J.-F. Carlin, A. Georgakilas, and D. Pogany, IEEE Trans. Electron Devices **53**, 422, (2006).

[3] F. Medjdoub, J.-F. Carlin, M. Gonschorek, E. Feltin, M.A. Py, D. Ducatteau, C. Gaquière, N. Grandjean, and E. Kohn, IEDM Tech. Dig., 2006, p.1.

[4] M. Miyoshi, Y. Kuraoka, M. Tanaka, and T. Egawa, Appl. Phys. Express **1**, 081102 (2008).

[5] M. Miyoshi, T. Tsutsumi, G. Nishino, Y. Miyachi, M. Okada, and J. J. Freedsman, and T. Egawa, J. Vac. Sci. Technol. B **34**, 050602 (2016).

[6] S.Choi, H. J. Kim, S-S. Kim, J. Liu, J. Kim, J-H. Ryou, R. D. Dupuis, A. M. Fischer, and F. A. Ponce, Appl. Phys. Lett. **96**, 221105 (2010).

[7] Y-Y. Zhang, X-L. Zhu, Y-A. Yin, and J. Ma, IEEE Electron Device Lett. **33**, 994 (2012).

[8] H. Isihikawa, T. Jimbo, and T. Egawa, Phys. Stat. Sol. C **5**, 2086 (2008).

[9] K. Ikeyama, Y. Kozuka, K. Matsui, S. Yoshida, T. Akagi, Y. Akatsuka, N. Koide, T. Takeuchi, S. Kamiyama, M. Iwaya, and I. Akasaki, Appl. Phys. Express **9**, 102101 (2016).

[10] G. Cosendey, A. Castiglia, G. Rossbach, J.-F. Carlin, and N. Grandjean. Appl. Phys. Lett. **101**, 151113 (2012)

[11] H. P. D. Schenk, M. Nemoz, M. Korytov, P. Vennéguès, A. D. Dräger, and A. Hangleiter, Appl. Phys. Lett. **93**, 08116 (2008).

[12] T. Frost, A. Hazari, A. Aiello, M. Z. Baten, L. Yan, J. Mirecki-Millunchick, and P. Bhattacharya, Jpn. J. Appl. Phys. **55**, 032101 (2016).

[13] A. Castiglia, E. Feltin, J. Dorsaz, G. Cosendey, J.-F. Carlin, R. Butté, and N. Grandjean, Electronics Lett. **44**, 521 (2008).

[14] S. Senda, H. Jiang, and T. Egawa, Appl. Phys. Lett. **92**, 203507 (2008).

[15] L.Li, D. Hosomi, Y. Miyachi, T. Hamada, M. Miyoshi, and T. Egawa, Appl. Phys. Lett. **111**, 102106 (2017).

[16] A. Lupu, F. H. Julien, S. Golka, G. Pozzovivo, G. Strasser, E. Baumann, F. Giorgetta, D. Hofstetter, S. Nicolay, M. Mosca, E. Feltin, J.-F. Carlin, and N. Grandjean, IEEE Photonics Technol. Lett. **20**, 102 (2008).

[17] S. Nakamura, Solid State Commun. **102**, 237 (1997).

[18] S. Nakamura, M. Senoh, S. Nagahama, N. Iwasa, T. Yamada, T. Matsushita, H. Kiyoku, Y. Sugimoto, T. Kozaki, H. Umemoto, M. Sano, K. Chocho, J. Cryst. Growth 189–190, 820 (1998).

[19] T. Aschenbrenner, H. Dartsch, C. Kruse, M. Anastasescu, M. Stoica, M. Gartner, A. Pretorius, A. Rosenauer, T. Wagner, and D. Hommel, J. Appl. Phys. **108**, 063533 (2010).

[20] M. Miyoshi, M. Yamanaka, T. Egawa, and T. Takeuchi, Applied Physics Express **11**, 051001 (2018).

[21] T. Takeuchi, H. Takeuchi, S. Sota, H. Sakai, H. Amano, and I. Akasaki, Jpn. J. Appl. Phys. **36**, L177 (1997).

[22] R. R. Pelá, C. Caetano, M. Marques, L. G. Ferreira, J. Furthmüller, and L. K. Teles, Appl. Phys. Lett. **98**, 151907 (2011).

[23] J. Dion, Q. Fareed, B. Zhang, and A. Khan, J. Electron. Mater. **40**, 377 (2011).

[24] M. Shur, M. Shatalov, A. Dobrinsky, and R. Gaska, in *GaN and ZnO-Based Materials and Devices*, ed. S. Pearton (Springer, Heidelberg 2012) Springer Series in Materials Science, Vol. 156, p.83.

[25] F. Bernardini, V. Fiorentini, and D. Vanderbilt, Phys. Rev. B **63**, 193201 (2001).

[26] V. Darakchieva, M. Beckers, M.-Y. Xie, L. Hultman, B. Monemar, J.-F. Carlin, E. Feltin, M. Gonschorek, and N. Grandjean, J. Appl. Phys. **103**, 103513 (2008).

[27] Z. L. Miao, T. J. Yu, F. J. Xu, J. Song, L. Lu, C. C. Huang, Z. J. Yang, X. Q. Wang, G. Y. Zhang, X. P. Zhang, D. P. Yu, and B. Shen, J. Appl. Phys. 107, 043515 (2010).

[28] G. Perillat-Merceroz, G. Cosendey, J-F. Carlin, R. Butté, and N. Grandjean, J. Appl. Phys. **113**, 063506 (2013).

[29] S. Kret, A. Wolska, M. T. Klepka, A. Letrouit, F. Ivaldi, A. Szczepańska, J.-F. Carlin, N. A. K. Kaufmann, and N. Grandjean, J. Phys: Conference series **326**, 012013 (2011).

[30] Z. T. Chen, K. Fujita, J. Ichikawa, and T. Egawa, J. Appl. Phys. **111**, 053535 (2012).

[31] Q. Y. Wei, T. Li, Y. Huang, J. Y. Huang, Z. T. Chen, T. Egawa, and F. A. Ponce, Appl. Phys. Lett. **100**, 092101 (2012).

[32] K. Lorenz, N. Franco, E. Alves, S. Pereira, I. M. Watson, R. W. Martin, and K. P. O'Donnell, J. Crys. Growth **310**, 4058 (2008).

[33] A Redondo-Cubero, K Lorenz, R Gago, N Franco, M-A di Forte Poisson, E Alves, and E Muñoz, J. Phys. D: Appl. Phys. **43**, 055406 (2010).

[34] P. Vennégues, B. S. Diaby, H. Kim-Chauveau, L.Bodiou, H .P .D. Schenk, E. Frayssinet, R.W. Martin, I. M. Watson, J. Cryst. Growth **353**, 108 (2012).

[35] R. People and J. C. Bean, Appl. Phys. Lett. **47**, 322 (1985); 49, 229 (1986).

[36] J. W. Matthews and A. E. Blakeslee, J. Cryst. Growth 27, **118** (1974).

[37] J. Tauc, R. Grigorovici, and A. Vancu, Phys. Stat. Solidi B **15**, 627 (1966).

[38] M. J. Lukitsch, Y. V. Danylyuk, V. M. Naik, C. Huang, G. W. Auner, L. Rimai, and R. Naik, Appl. Phys. Lett. **79**, 632 (2001).

[39] T. Peng, J. Piprek, G. Qiu, J. O. Olowolafe, K. M. Unruh, C. P. Swann, and E. F. Schubert, Appl. Phys. Lett. **71**, 2439 (1997).

[40] Q. Guo, K. Yahata, T. Tanaka, M. Nishio, and H. Ogawa, Phys. Status Solidi **C 0**, 2533 (2003).

[41] S. Yamaguchi, M. Kariya, S. Nitta, T. Takeuchi, C. Wetzel, H. Amano, and I. Akasaki, Appl. Phys. Lett. **73**, 830 (1998).

[42] K. S. Kim, A. Saxler, P. Kung, M. Razeghi, and K. Y. Lim, Appl. Phys. Lett. **71**, 800 (1997).

[43] M. Goano, E. Bellotti, E. Ghillino, C. Garetto, G. Ghione, and K. F. Brennan, J. Appl. Phys. **88**, 6476 (2000).

[44] J. Wu, J. Appl. Phys. **106**, 011101 (2009).

Figure captions

Fig. 1. Compositional dependence of RMS surface roughness for 300-nm-thick AlInN films. Typical surface AFM images are also shown.

Fig. 2. Compositional dependence of (a) in-plane lattice constant a and (b) in-plane lattice strain ε_{xx} for 300-nm-thick AlInN films. Blue solid line shows calculated in-plane lattice constant for perfectly-relaxed AlInN crystals.

Fig. 3. Cross-sectional TEM bright-field images and XRD ω-2θ (0002) profiles for AlInN/GaN structures with InN molar fractions of (a) 0.164 and (b) 0.197.

Fig. 4. Results of cross-sectional scanning transmission electron microscope (STEM) observation and EDS analysis for the AlInN film with an InN molar fraction of 0.197. That is, (a) the cross-sectional STEM image, the EDS elemental maps for (b) Al and (c) In in the same view field as that of STEM, and (d) the result of the EDS line analysis.

Fig. 5. Critical thicknesses for epitaxial AlInN films calculated according to the People-Bean's (red lines) and Matthews-Blakeslee's (blue lines) expressions [34,35]. Experimental results obtained in this study are also plotted with brief comments.

Fig. 6. (a) Compositional dependence of XRC-FWHMs for 300-nm-thick AlInN films, and typical XRC profiles for AlInN films with InN molar fractions of (b) 0.114, (c) 0.164 and (d) 0.197.

Fig. 7. Spectra of (a) refractive index n and (b) extinction coefficient k for 300-nm-thick AlInN films with various alloy compositions.

Fig. 8. (a) Absorption spectra for different-alloy-composition AlInN films grown on c-plane GaN on sapphire. (b) Relationship between energy bandgaps and alloy compositions for AlInN, in which previously reported data are also plotted. This figure is made by updating a figure organized by Aschenbrenner *et al* [19].

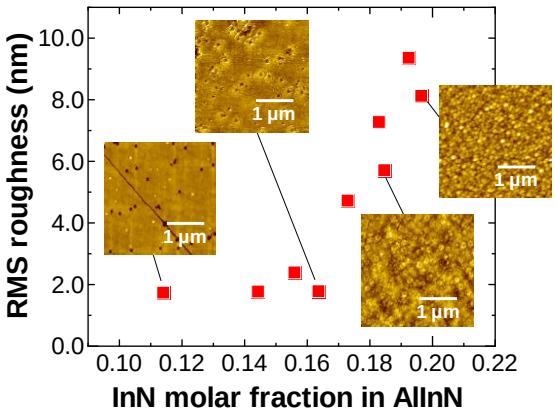
RMS roughness (nm)
10.0
8.0
6.0
4.0
2.0
0.0
0.10
0.12
0.14
0.16
0.18
0.20
0.22
InN molar fraction in AlInN
1 µm
1 µm
1 µm
1 µm

Fig. 1

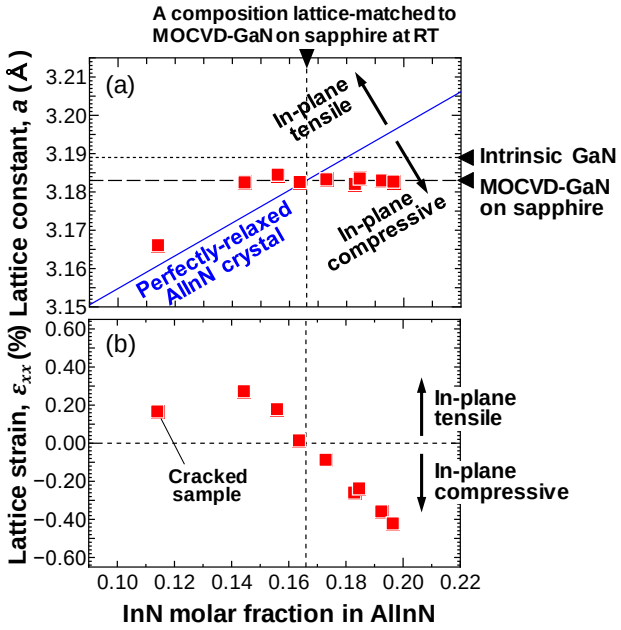
A composition lattice-matched to
MOCVD-GaN on sapphire at RT
(a)
(b)
In-plane
tensile
In-plane
compressive
Intrinsic GaN
MOCVD-GaN
on sapphire
Perfectly-relaxed
AlInN crystal
Cracked
sample
In-plane
tensile
In-plane
compressive
Lattice constant, a (Å)
Lattice strain, ε_{xx} (%)
InN molar fraction in AlInN
3.21
3.20
3.19
3.18
3.17
3.16
3.15
0.60
0.40
0.20
0.00
−0.20
−0.40
−0.60
0.10
0.12
0.14
0.16
0.18
0.20
0.22

Fig. 2

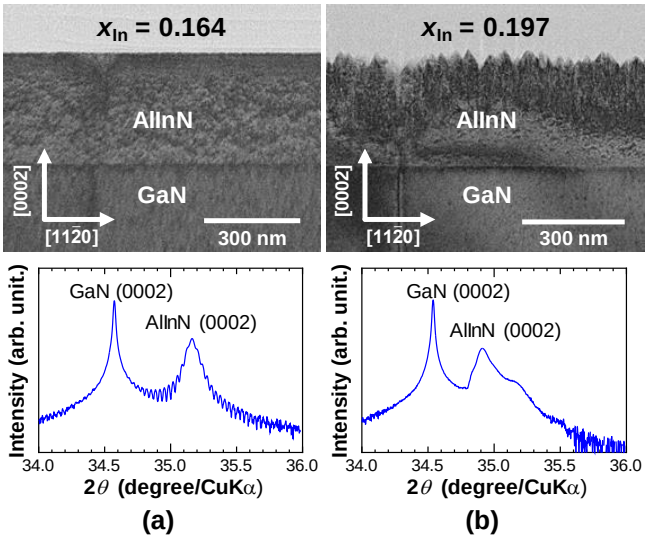
x_{In} = 0.164
AlInN
GaN
[0002]
[11$\bar{2}$0]
300 nm
x_{In} = 0.197
AlInN
GaN
[0002]
[11$\bar{2}$0]
300 nm
Intensity (arb. unit.)
GaN (0002)
AlInN (0002)
34.0
34.5
35.0
35.5
36.0
2θ (degree/CuKα)
(a)
Intensity (arb. unit.)
GaN (0002)
AlInN (0002)
34.0
34.5
35.0
35.5
36.0
2θ (degree/CuKα)
(b)

Fig. 3

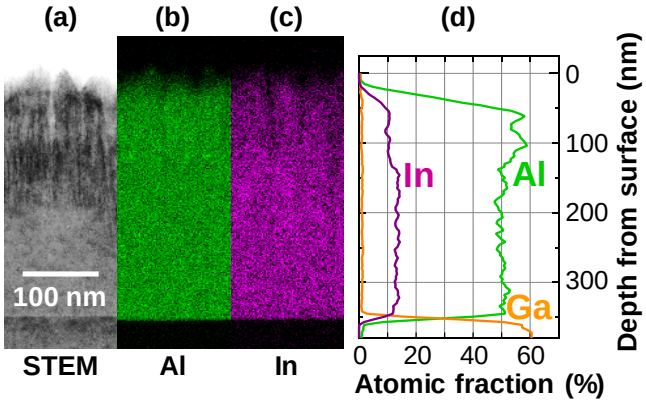
(a)
(b)
(c)
(d)
100 nm
STEM
Al
In
In
Al
Ga
0
100
200
300
Depth from surface (nm)
0
20
40
60
Atomic fraction (%)

Fig. 4

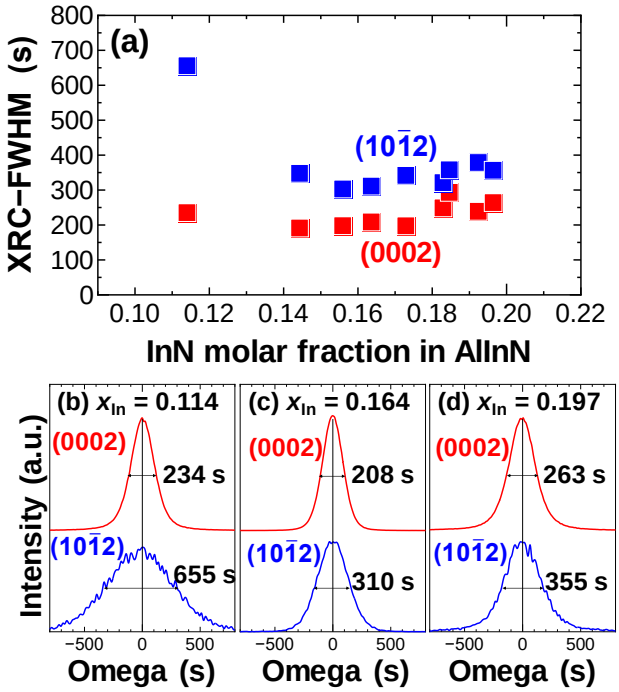
(a)
XRC−FWHM (s)
InN molar fraction in AlInN
(10$\bar{1}$2)
(0002)
(b) x_{In} = 0.114
(c) x_{In} = 0.164
(d) x_{In} = 0.197
Intensity (a.u.)
234 s
655 s
208 s
310 s
263 s
355 s
Omega (s)

Fig. 5

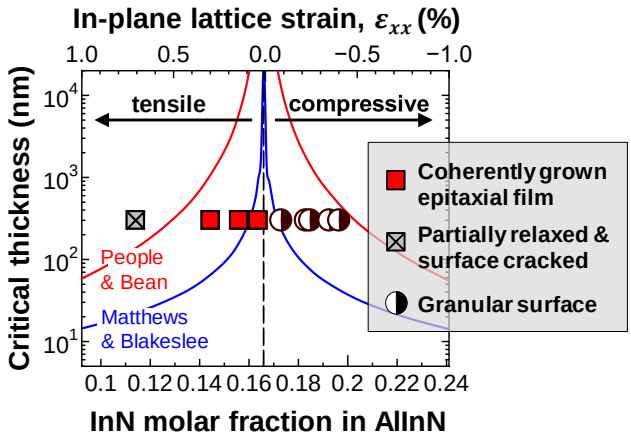
In-plane lattice strain, ε_{xx} (%)
1.0
0.5
0.0
−0.5
−1.0
Critical thickness (nm)
10^4
10^3
10^2
10^1
tensile
compressive
People
& Bean
Matthews
& Blakeslee
Coherently grown
epitaxial film
Partially relaxed &
surface cracked
Granular surface
0.1
0.12
0.14
0.16
0.18
0.2
0.22
0.24
InN molar fraction in AlInN

Fig. 6

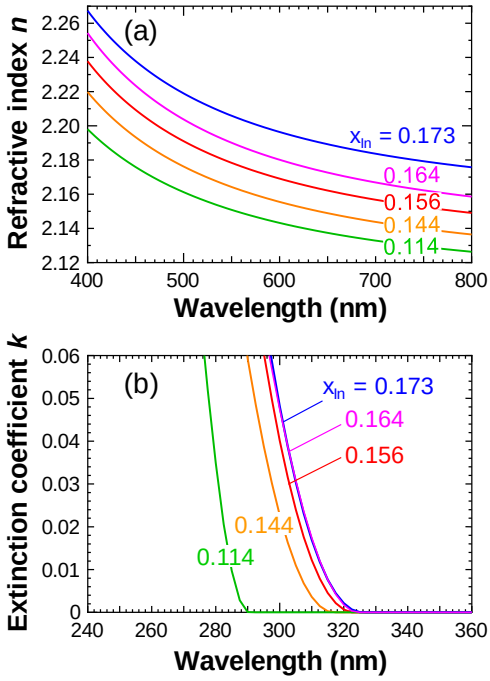
(a)
Refractive index n
2.26
2.24
2.22
2.20
2.18
2.16
2.14
2.12
400
500
600
700
800
Wavelength (nm)
x_In = 0.173
0.164
0.156
0.144
0.114
(b)
Extinction coefficient k
0.06
0.05
0.04
0.03
0.02
0.01
0
240
260
280
300
320
340
360
Wavelength (nm)
x_In = 0.173
0.164
0.156
0.144
0.114

Fig. 7

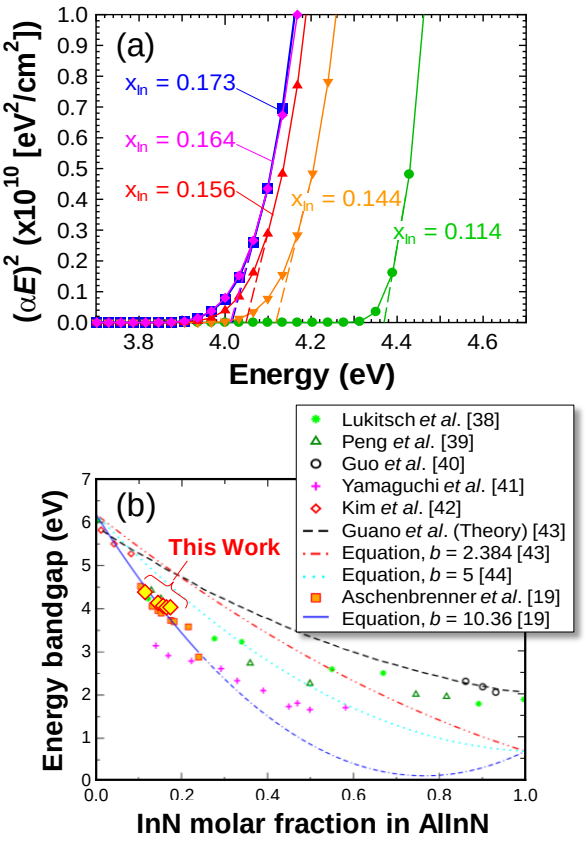
(a)
x_{In} = 0.173
x_{In} = 0.164
x_{In} = 0.156
x_{In} = 0.144
x_{In} = 0.114
$(\alpha E)^2$ (x10^{10} [eV^2/cm^2])
Energy (eV)
(b)
This Work
Lukitsch *et al*. [38]
Peng *et al*. [39]
Guo *et al*. [40]
Yamaguchi *et al*. [41]
Kim *et al*. [42]
Guano *et al*. (Theory) [43]
Equation, *b* = 2.384 [43]
Equation, *b* = 5 [44]
Aschenbrenner *et al*. [19]
Equation, *b* = 10.36 [19]
Energy bandgap (eV)
InN molar fraction in AlInN

Fig. 8